RSC Advances

PAPER

View Article Online
View Journal | View Issue

Cite this: *RSC Adv.*, 2023, **13**, 20150

Alginate@$ZnCO_2O_4$ for efficient peroxymonosulfate activation towards effective rhodamine B degradation: optimization using response surface methodology†

Badr-Eddine Channab, [a] Mohamed El Ouardi, [bc] Salah Eddine Marrane,[a] Omar Ait Layachi,[d] Ayoub El Idrissi, [a] Salaheddine Farsad, [e] Driss Mazkad,[f] Amal BaQais,[g] Mohammed Lasri [h] and Hassan Ait Ahsaine *[b]

A facile chemical procedure was utilized to produce an effective peroxy-monosulfate (PMS) activator, namely $ZnCo_2O_4$/alginate. To enhance the degradation efficiency of Rhodamine B (RhB), a novel response surface methodology (RSM) based on the Box–Behnken Design (BBD) method was employed. Physical and chemical properties of each catalyst ($ZnCo_2O_4$ and $ZnCo_2O_4$/alginate) were characterized using several techniques, such as FTIR, TGA, XRD, SEM, and TEM. By employing BBD-RSM with a quadratic statistical model and ANOVA analysis, the optimal conditions for RhB decomposition were mathematically determined, based on four parameters including catalyst dose, PMS dose, RhB concentration, and reaction time. The optimal conditions were achieved at a PMS dose of 1 g l^{-1}, a catalyst dose of 1 g l^{-1}, a dye concentration of 25 mg l^{-1}, and a time of 40 min, with a RhB decomposition efficacy of 98%. The $ZnCo_2O_4$/alginate catalyst displayed remarkable stability and reusability, as demonstrated by recycling tests. Additionally, quenching tests confirmed that $SO_4^{\bullet-}$/$OH^{\bullet}$ radicals played a crucial role in the RhB decomposition process.

Received 30th April 2023
Accepted 17th June 2023

DOI: 10.1039/d3ra02865h

rsc.li/rsc-advances

1 Introduction

Organic dyes play a crucial role in various industries, including cosmetics, pharmaceutical, textiles, papermaking, plastics, and food.[1,2] According to recent studies, an estimated 100 tons per year of colorants are discharged into aquatic ecosystems, despite the annual consumption of over 104 tons per year, primarily stemming from the textile sector.[3] The intricate structure of organic dyes, particularly those utilized in the textile industry, can be carcinogenic and mutagenic, leading to severe ecological challenges when disposed of in industrial wastewater. In anaerobic conditions, toxic aromatic amines can form, exacerbating the issue.[4]

For this purpose, researchers are researching new approaches and new functional materials for the removal of pollutants. Adsorption involves the removal of contaminants by attracting and binding them to a solid surface. It offers advantages such as high efficiency, simplicity, and versatility.[5] However, it may require frequent replacement or regeneration of adsorbents and may be limited in capacity and selectivity. Photocatalysis uses light-activated catalysts to degrade contaminants and offers advantages such as rapid degradation rates, the potential for mineralization, and versatility in treating a wide range of contaminants. However, it can be hindered by catalyst stability, limited light penetration, and the formation of potentially toxic by-products.[6,7] Microwave catalysis uses microwave energy to generate heat for enhanced contaminant degradation. It offers advantages like rapid reaction kinetics, energy efficiency, and scalability.[8,9] However, challenges include careful optimization of operating conditions and the potential for heating non-target compounds. SR-AOPs have become

[a]*Laboratory of Materials, Catalysis & Natural Resources Valorization, URAC 24, Faculty of Science and Technology, Hassan II University, B.P. 146, Casablanca, Morocco*

[b]*Laboratory of Applied Materials Chemistry, Faculty of Sciences, MohammedV University in Rabat, Morocco. E-mail: mohamed.elouardi@um5r.ac.ma*

[c]*Aix Marseille University, University of Toulon, CNRS, IM2NP, CS 60584, CEDEX 9, F-83041 Toulon, France*

[d]*Laboratory of Physical Chemistry and Biotechnology of Biomolecules and Materials, Faculty of Sciences and Technology, Hassan II University of Casablanca, Mohammedia 20650, Morocco*

[e]*Materials and Environment Laboratory, Ibn Zohr University, Agadir, 8000, Morocco*

[f]*Laboratory of Spectroscopy, Molecular Modeling, Materials, Nanomaterials, Water and Environment, Materials for Environment Team, ENSAM, Mohammed V University in Rabat, Morocco*

[g]*Department of Chemistry, College of Science, Princess Nourah Bint Abdulrahman University, P.O. Box 84428, Riyadh 11671, Saudi Arabia*

[h]*Laboratoire of Applied Chemistry and Biomass, Department of Chemistry, Faculty of Sciences, University Cadi Ayyad, Semlalia, BP 2390 Marrakech, Morocco*

† Electronic supplementary information (ESI) available. See DOI: https://doi.org/10.1039/d3ra02865h

extremely popular due to their remarkable adaptability and efficacy in purifying and breaking down substances. These processes involve the generation of sulfate radicals ($SO4^{\bullet -}$) *via* persulfate (PS) and peroxy-disulfate (PDS, $S_2O_8^{2-}$), or the co-production of sulfate and hydroxyl radicals ($HO^{\bullet}$) *via* peroxymonosulfate (PMS, HSO_5^{-}), as well as their redox potential (2.5–3.1 V *vs.* NHE), which surpasses that of the hydroxyl radical (1.9–2.7 V *vs.* NHE). Furthermore, these methods offer high stability and can operate over a wide pH range (3–9).[10,11] There are several methods for the activation of PMS, namely thermal process, ultrasound, UV irradiation and transition metals.[12] In particular, the activation of PMS by heterogeneous transition metal catalysts has attracted considerable attention owing to their excellent catalytic ability for the rapid decomposition of a wide variety of pollutants.[13,14] Over the past few years, many researchers have been developing many catalysts based on tungstates,[15] oxides,[16,17] vanadates,[18,19] metal–organic frameworks[20] for the decomposition of various organic pollutants as well as sewage treatment. Besides these materials, cobalt-based spinels (MCo_2O_4 where M = Cu, Zn, Fe, Ni, *etc.*), based on their catalytic and structural properties, have received much attention in the degradation of organic pollutants. According to literature, various kinds of ternary spinels such as $CuCo_2O_4$,[21] $NiCo_2O_4$,[22,23] $MnCo_2O_4$,[24] have been studied intensively as catalysts for PMS activation and decomposition of organic pollutants. Of the above, $ZnCo_2O_4$ has a normal spinel structure, with Zn^{2+} being located in the centers of the tetrahedral coordinate positions (Td), and Co^{3+} occupies the octahedral environment. Hence, in comparison to Co_3O_4, using $ZnCo_2O_4$ may reduce the rare and relatively costly element Co without any compromise in catalytic activity.[25,26] For these reasons, Hu *et al.*[27], developed another efficient peroxymonosulfate (PMS) activator, $ZnCo_2O_4$, *via* a microwave-assisted procedure for the degradation of bisphenol A in aqueous solutions. They reported a degradation efficacy of 99.28% that was achieved within 5 min under the following conditions ($ZnCo_2O_4$: 0.2 g l^{-1}) and $[PMS]/[BPA]_{molar} = 2$. Similarly, Gao *et al.*[28], succeeded in fabricating a three-dimensional $ZnCo_2O_4$ catalyst through a hydrothermal approach which was eventually employed as persulfate (PS) activators by microwave irradiation to degrade levofloxacin (LVF). A removal of LVF of 69.8% within 40 min was recorded by TOC technique at $[pH]_0 = 5$, [LVF] = 10 ppm, [PS] = 5 mM, [ZCO] = 2 g l^{-1}, $T = 70$ °C and MW = 700 W. Recently, the same team.[29], examined the degradation of ciprofloxacin (CIP) using persulfate (PS) activated with the 3D hybrid C@$ZnCo_2O_4$. The radical trapping investigation indicated that the radicals responsible for CIP degradation under the microwave irradiation process were $SO_4^{\bullet -}$, $OH^{\bullet}$ and $O_2^{\bullet -}$, moreover under conditions of [PS] = 0.25 Mm, [C@$ZnCo_2O_4$] = 1.5 g l^{-1}, MW = 600 W, $T = 40$ °C and $[pH]_0 = 6.5$, the CIP removal rate was 90% during 40 min.

Nevertheless, the use of powdered materials has delayed their applications for small-scale sewage treatment and their commercialization primarily because of the difficulty of recovery and recycling of fine nanoparticles.[30] As a result, it seems that encapsulating small materials in a biopolymeric matrix would be a favorable approach for both simpler recovery and increased adsorption capabilities.[31,32] The most appropriate biopolymers that have attracted the attention of researchers is alginate.[33] Alginate is a natural polymer that is highly biocompatible, relatively inexpensive, non-toxic, biodegradable, and renewable, making it an excellent adsorbent for both organic and inorganic pollutants that can be extracted from brown algae and bacteria. This linear polysaccharide is composed of b-D-mannuronic acid and a-L-guluronic acid monomers arranged in a non-regular and blockwise manner along the chain.[34] Additionally, alginate can create stable hydrogels due to the strong junctions formed between the G blocks and divalent cations based on the "egg-box" model.[35] Moreover, its carboxylate function endows alginate with a negative charge, transforming it into a useful polyelectrolyte that can conveniently capture cationic dyes, such as Rhodamine B (RhB), primarily through strong electrostatic interactions that enhance the contact between rhodamine B and $ZnCo_2O_4$.[36] On the other hand, the pollutant degradation process involves a lot of experimental factors interacting in a non-linear manner. In this situation, the traditional approach of dye degradation optimization becomes ineffective as it takes a lot of experimental tests and time. Furthermore, this approach fails to depict the interaction effects of all operational parameters implicated in the degradation pathway. In an effort to surmount these setbacks, researchers are relying on statistically based experimental designs such as surface response methodology (RSM) to achieve effective optimization of the degradation process.[37,38] RSM is viewed as a robust statistical method to design experiments, establish models by examining the influence of multiple process parameters by changing them simultaneously.[39,40] Thus, the ultimate goal of using RSM is to determine the optimal operating conditions within a brief period of time and a few experiments. Among the different matrix designs the BBD consists of an incomplete three-level factorial design. The totality of the experiments is reduced into a quadratic fitting model which is excellent for accurately expressing linear interactions and quadratic effects. For example, Bouzayani *et al.*[41], highlighted the usefulness of RSM-BBD as a statistical method to enhance and optimise the catalytic oxidation process of Direct red 111 dye effluents. Three several factors were considered in the optimization procedure, namely the concentration of PMS, the catalyst dose, and the temperature. The purpose of this study is to prepare novel bio-nanocomposite beads based on $ZnCo_2O_4$/Ca-Alg *via* a simple, fast and green procedure, then investigate their efficiency in the degradation of RhB from aqueous solution as a new hybrid process. The RhB degradation was optimized by varying four operating variables namely the RhB initial concentration, the catalyst dose, the PMS dose and the contact time using Box–Behnken Design (BBD). Kinetics, pH and temperature effects on the degradation process were also examined to gain insight into the degradation mechanisms. The reuse of our prepared material was also studied. The outcomes of this study will help further to develop an eco-friendly biocomposite for the large-scale sewage treatment.

2 Materials and methods

2.1. Chemicals and reactants

Cobalt(II) chloride ($CoCl_2$), zinc nitrate hexahydrate ($Zn(NO_3)_2 \cdot 6H_2O$), calcium chloride ($CaCl_2$), oxalic acid ($C_2H_2O_4$), potassium peroxymonosulfate ($KHSO_5$), nitric acid (HNO_3), sodium hydroxide (NaOH), rhodamine B ($C_{28}H_{31}ClN_2O_3$) were bought from Sigma-Aldrich. Sodium alginate (Na-Alg), NaOH, ethanol, H_2O_2 and *tert*-butanol (TBA), PEG400 were obtained from VWR Chemicals. All of these reagents were of high analytical quality and were operated without any additional purification.

2.2. $ZnCo_2O_4$ manufacturing

Fig. 1a shows the operating procedure followed to elaborate our sample, first of all 0.297 g of $Zn(NO_3)_2 \cdot 6H_2O$, 0.582 g of $CoCl_2$ were dissolved in 10 ml EtOH, and 10 ml PEG400, the remaining solution has been agitated for 30 minutes. Secondly, 0.63 g of oxalic acid was dispersed in 10 ml of EtOH, and after the obtained solution has been added drop by drop to the previous solution and stir for 1 h until a pink precipitate is obtained. The precipitate as formed centrifugally separated, and it was cleaned with distilled water and EtOH three times, followed by drying at 70 °C for 24 h in an oven. Then, the resulting powder has been treated at 450 °C for 4 h.

2.3. Nanocomposite-beads preparation

The $ZnCo_2O_4$(ZCO) nano-material has been immobilized on calcium alginate beads using ionotropic gelation (Fig. 1b). Briefly, 0.5 g of $ZnCo_2O_4$ is dispersed in 100 ml of distilled water, using an ultrasonic apparatus (Hielscher, 400W), for 15 min, then 1 g of sodium alginate (Alg) is added, stirring for 12 h, with low agitation. The as-prepared hydrogel nanocomposite (ZCO/Alg), was added to $CaCl_2$ solution (1% W/V), through a peristaltic pump. To get uniformly sized spherical beads. The prepared beads have been kept overnight in the $CaCl_2$ solution at 4 °C for the curing. Subsequently, the prepared beads were harvested, cleaned with distilled water to remove excess of Ca^{2+}.

2.4. Material characterizations

Several structural and spectroscopic techniques were employed to study the resulting catalyst. X-ray diffraction (XRD) using Cu Kα radiation ($\lambda = 0.15406$ nm) and a Bruker D8 Advance Twin instrument was used to identify the phases present in the sample, with a scan range of 10 to 80°. The morphology was studied by scanning electron microscopy (SEM) using a Jeol JSM-6460LAV instrument with an energy dispersive X-ray spectrometer (EDS) at 20 kV. Transmission electron microscopy (TEM) was also used to register images and selected area electron diffraction (SAED) patterns, using a JEM-2100F transmission electron microscope. Fourier-transform infrared attenuated total reflection (FTIR-ATR) analysis was carried out on sample pellets with KBr using a Shimadzu spectrometer, in the wavenumber range of 400 to 4000 cm^{-1}. Thermogravimetric analysis (TGA) was performed in air using a DTG-60 SHIMADZU apparatus, heating approximately 22 mg of sample from 25 °C to 500 °C while registering weight variation *versus* temperature. The pH zero-point charge (pH_{zpc}) of the $ZnCo_2O_4$/Alg and Alg wet beads was determined using a method described by Wan

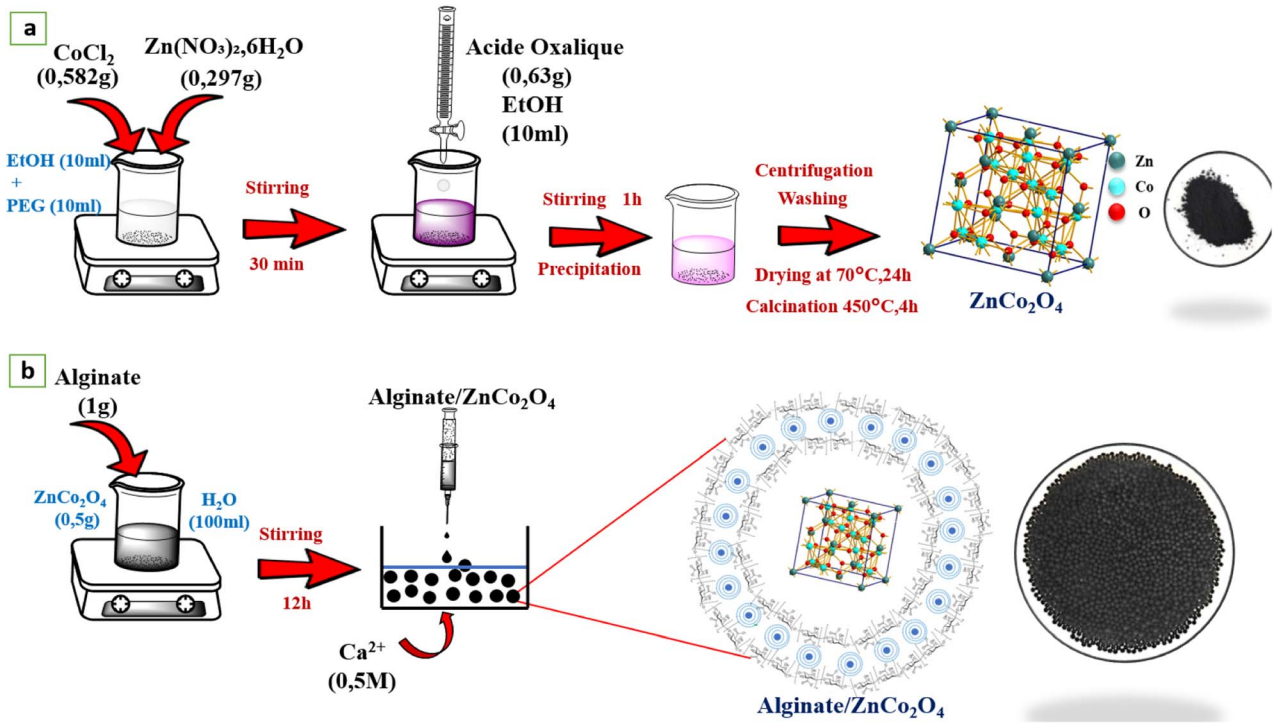

Fig. 1 (a) Preparation of the $ZnCo_2O_4$ powder, (b) $ZnCo_2O_4$/alginate composite.

Ngah *et al.*[42] Wet beads weighing approximately 250 mg were added to 50 ml of 0.1 M $NaNO_3$, and the pH of the solution was adjusted to between 2 and 13 using 0.1 M HCl and 0.1 M NaOH.

2.5. Catalytic procedure

Rhodamine B (RhB) degradation tests were executed in a 50 ml beaker at room temperature. The test bath contains the solution to be degraded of concentration 25 mg l^{-1} with a certain quantity of the catalyst. The mixture was vigorously agitated for 1 h to achieve an adsorption–desorption equilibrium between RhB and the catalyst. Afterwards an amount of PMS was introduced to the solution to initiate the decomposition reaction. During the decomposition reaction a volume of 1.5 ml was taken after each 5 min to follow the variation of the absorbance by using the UV-vis 6705 spectrophotometer. It is well noted that the absorption band of RhB is 554 nm. The measurement of Chemical Oxygen Demand (COD) determines the overall amount of oxygen required to oxidize organic molecules into CO_2 and H_2O. To measure COD, the closed reflux method was employed using $K_2Cr_2O_7$ as the oxidizing agent in an acidic environment, following by a colorimetric analysis, and the results were analyzed using UV-vis 6705 spectrophotometer.

The degradation rate was reported as COD_t/COD_0 *versus* time. This rate was calculated for various reaction times according to the following relation:

$$\mathrm{COD}(\%) = \left(\frac{\mathrm{COD}_0 - \mathrm{COD}_t}{\mathrm{COD}_0}\right) \times 100 \quad (1)$$

COD_0: COD concentration (mg l^{-1} of O_2) at initial time (before degradation), COD_t: COD concentration (mg l^{-1} of O_2) at a value of time t.

2.6. BBD-RSM design and data analysis

The optimization of RhB degradation efficiency was carried out in this study using the Box–Behnken design coupled with surface response methodology. To optimize the four selected parameters that affect the variations of RhB degradation efficiency when using $ZnCo_2O_4$/CaAlg beads as a catalyst, a three-level factorial design was employed, which involved a total of 30 experiments. These factors were selected on the basis of literature reports for organic dyes degradation as well as the results of initial experiments conducted in the laboratory. The other factors, including temperature and pH of the RhB solution were set at 25 °C and 5.8 respectively. Table S1† shows the experimental domain with different level values of each factor.

Using the Nemrodw software, the experimental design data was analyzed and a polynomial quadratic model, represented by the following equation, was used to fit the responses (RhB degradation-efficiency):

$$\hat{Y} = b_0 + \sum_{i=1}^{n} b_i X_i + \sum_{i=1}^{n} b_{ii}\ {X_i}^2 + \sum_{i=1}^{n-1} b_{ij} X_i X_j + \varepsilon \quad (2)$$

The predicted response ($\hat{Y}$) was determined based on the regression coefficients for the intercept (b_0), linear (b_i), quadratic (b_{ii}), and interaction (b_{ij}) terms between the input variables. The levels of the independent factors in coded units were represented by X_i, ${X_i}^2$, and X_j. To determine the statistical significance of the regression model, an analysis of variance (ANOVA) was performed. Additionally, 2D–3D surface plots were generated to identify the optimal operating conditions for achieving high RhB degradation.

3 Results and discussion

3.1. Structural analysis

To identify key changes (vibrational modes, functional groups, and behavior) in the materials, the FTIR was used. The FTIR spectrum of the $ZnCo_2O_4$ spinel is shown in Fig. 2a. As can be seen, there is a strong absorption bands at 665 cm^{-1} and 568 cm^{-1} which are assigned to the metal–oxygen bond vibrations of the synthesized material at the tetrahedral and octahedral coordinating metal ions, respectively.[43,44] It is confirmed by the absence of an absorption band in the region of higher wavenumbers that organic materials, which were used during the synthesis process, are not present, revealing the successful synthesis of the $ZnCo_2O_4$ spinel. Fig. 2a, displays the spectrum of the characteristic bands of the sodium alginate molecule (NaAlg). The vibrational FTIR spectrum of NaAlg displays various peaks indicating the stretching vibrations of different chemical groups. Specifically, the absorption bands at 868 cm^{-1} and 911 cm^{-1} are associated with the stretching vibration of Na–O,[45] while the peak at 1035 cm^{-1} is attributed to the stretching vibration of C–O of the COO– and the alcohol groups (–C–OH) present in the polysaccharide structure of NaAlg.[46,47] Moreover, the absorption bands at 1601 cm^{-1} and 1407 cm^{-1} correspond to asymmetric and symmetric stretching vibrations of the carboxylate groups (–COO–), respectively.[48] The broad peak observed at 3321 cm^{-1} is due to the hydroxyl (O–H) stretching vibration mode.[49] These same peaks are also present in the FTIR spectrum of the NaAlg/$ZnCo_2O_4$ nanocomposite, indicating that the sodium alginate has bound to the surface of $ZnCo_2O_4$ and confirming the formation of $ZnCo_2O_4$–NaAlg beads through surface modification. The XRD technique was utilized to determine the phase, crystallinity, and purity of the manufactured materials. The XRD patterns in Fig. 2b confirmed the formation of $ZnCo_2O_4$ composite in the sample with cubic structure. The peaks were numbered and indexed. The corresponding planes are (111), (022), (131), (222), (040), (242), (151), (044) (Table S2†). These planes confirmed the formation of spinel-like cubic structure. The Indexed planes confirmed a face-centered cubic structure with the space group $Fd\bar{3}m$. The XRD study's findings are consistent with JCPDS no. 96-591-0137. As shown in Table S2,† the Scherer formula was employed to identify the crystallite size of the nanoparticles, and the corresponding equation is:

$$D = k\lambda/(\beta\cos\theta) \quad (3)$$

This equation includes the X-ray wavelength represented by λ, the Scherer constant denoted by K, the diffraction angle indicated by θ, and the full width-half maximum (FWHM) denoted by β. The absence of additional peaks on the XRD

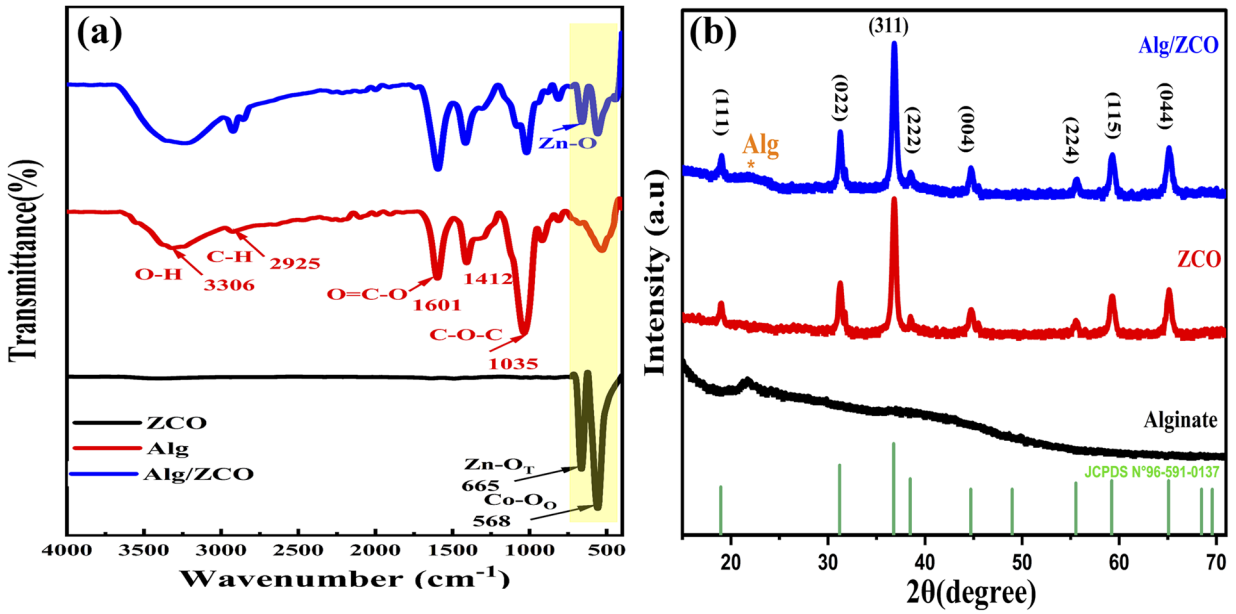

Fig. 2 (a) FTIR spectra of $ZnCo_2O_4$, NaAlg and NaAlg/$ZnCo_2O_4$. (b) XRD pattern of $ZnCo_2O_4$/Alg catalyst.

pattern indicated that the sample was pure, this corresponds to the FTIR result. The average value of crystallite size is founded to be 21.61 nm as well as the average calculated value for lattice parameters and cell volume ($a = 8.079$ A, $V = 527.617$ nm^3) are according to the theoretical values obtained of $ZnCo_2O_4$.[50] The XRD results for the alginate bead revealed the existence of a peak of $2\theta = 22°$,[51] this peak was also found in the ZCO/Alg composite which indicates the incorporation of ZCO into the alginate matrix. These results are in good agreement with the infrared results.

3.2. Surface morphology

The morphologies of the ZCO samples are explored using SEM and TEM. Fig. 3 displays SEM images at varying magnification of the ZCO calcined at 450 °C. As can be noticed in Fig. 3a and b, the surface morphological of the ZCO is porous and rough, additionally and due to the presence of oxalic acid complexing agent, the size of ZCO particles is not homogeneous.[43] Further information on ZCO morphologies and as we can have viewed in Fig. 3c and d The ZCO exhibits a porous architecture with freely stacked ZCO nanoflakes.[43] In Fig. 3e and f, the low-magnification TEM confirms that the nanoflakes ZCO are made up of uniform nanocrystals with a size of 15–5 nm. The lattice HRTEM picture of as-prepared ZCO is shown in Fig. 3g, demonstrating the great crystallinity of ZCO. The interplanar spacing of 0.461 nm is quite close to the normal d_{111} value of spinel $ZnCo_2O_4$ 0.4664 nm computed from the XRD data (Table S2†). The nano-crystalline character of the compound is indicated by the selected area electron diffraction (SAED) pattern (Fig. 3h), which consists of a clear, well-resolved set of concentric rings with occasional bright spots.[44,52] In addition, the morphological analysis and composition of the alginate-based beads were examined by SEM analysis and energy dispersive X-ray mapping (Fig. 3i–k). It is clearly marked that the mapping images confirm the existence of the characteristic elements of alginate (C, Ca, O). On the other hand, the composite images revealed that the ZCO material had been successfully introduced inside a membrane composed of calcium ions and alginate biopolymer, enabling the construction of spherical beads. Furthermore, mapping images confirm these results, which confirm the functionalization of ZCO nanoparticles by alginate/calcium (Fig. 3l and m). The EDS analysis (Fig. S1†) revealed the presence of characteristic peaks of each element corresponding to each material (ZCO powder, alginate, ZCO/Alg). These results are in good agreement with the infrared and XRD results.

3.3. Optimization and statistical analysis

In this study, the impact of four distinct factors on the efficacy of RhB decomposition was analyzed. These factors comprised catalyst dosage (X_1), PMS dosage (X_2), RhB initial concentration (X_3), and time (X_4). A total of 15 experiments were conducted to assess the impact of these four key independent variables on the percentage of RhB degradation efficiency (%). Table S3† lists the full matrix of experimental design for the four variables tested, as well as the observed (Y) and predicted ($\hat{Y}$) RhB degradation efficiency responses (%). To examine the interaction between the independent and dependent variables, a quadratic polynomial model was utilized. The predicted regression model for the RhB degradation efficiency response ($\hat{Y}$, %) is described below:

$$\begin{aligned}\hat{Y} = {} & 93.470 + 0.597X_1 - 0.197X_2 - 2.453X_3 - 11.663X_4 \\ & + 0.986X_1^2 - 1.758X_2^2 - 2.407X_3^2 - 3.587X_4 \\ & - 0.323X_1X_2 + 0.410X_1X_3 + 0.576X_2X_3 \\ & - 0.092X_1X_4 - 0.998X_2X_4 + 3.150X_3X_4 \end{aligned} \quad (4)$$

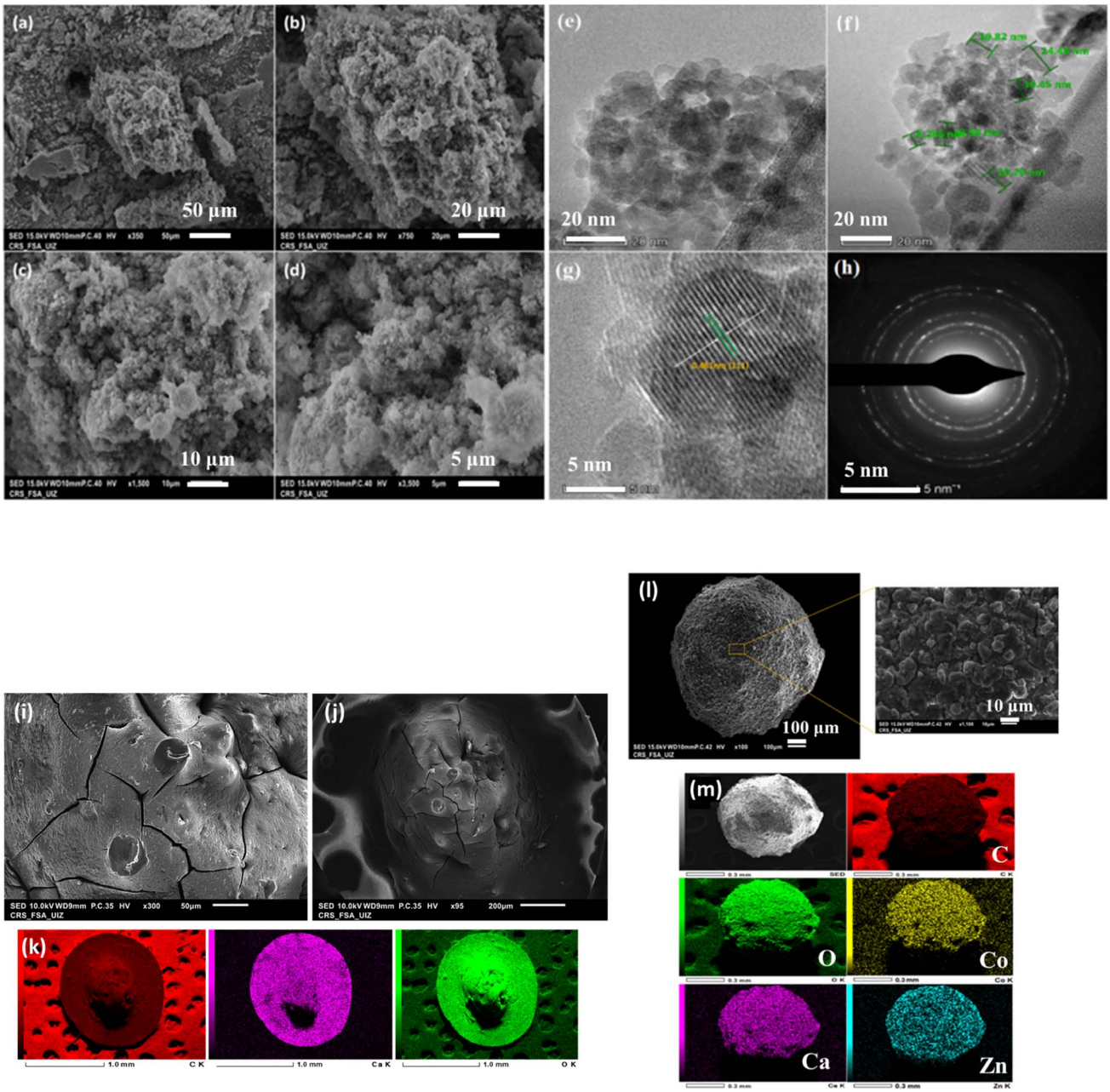

Fig. 3 (a–d) SEM images of $ZnCo_2O_4$ powder at different resolution. TEM (e and f) and (g) HR-TEM images of $ZnCo_2O_4$ powder, and (h) SAED pattern. (i–k) SEM images and mapping of Alg beads. (l and m) SEM images and mapping of Alg/ZCO beads.

The ANOVA was employed to evaluate and authenticate the significance of the quadratic polynomial model for the polynomial quadratic model.[53,54] The ANOVA results for RhB degradation efficiency are displayed in Table S4,† and the statistical significance of the model was determined by the *p*-value and *F*-value, where a *p*-value below 5% signifies that the model is statistically significant.[16,41] The output values of the model presented in Table S3† indicate a strong correlation between the experimental and predicted degradation efficiency (%). This correlation was further supported by the R^2 (0.984) and adjusted R^2 (0.969) values, as demonstrated in Fig. S5 (ESI†), which are closely linked and in excellent agreement for the quadratic model. This suggests that the quadratic polynomial model can accurately depict the connection between the process variables and response. Furthermore, the R^2 value of 0.984 reveals that the model accounts for 98.4% of the total variation in RhB degradation data. The ANOVA analysis (Table S4†) reveals that the mathematical model proposed in the study is statistically significant, with a *p*-value of 0.01% and an *F*-value of 66.470. The model fits well with the experimental data, as evidenced by the lack of fit being non-significant (Table S4†). The linear, quadratic, and interaction terms of the four factors (catalyst mass, PMS mass, initial RhB concentration, and contact time) were evaluated for their significance on the

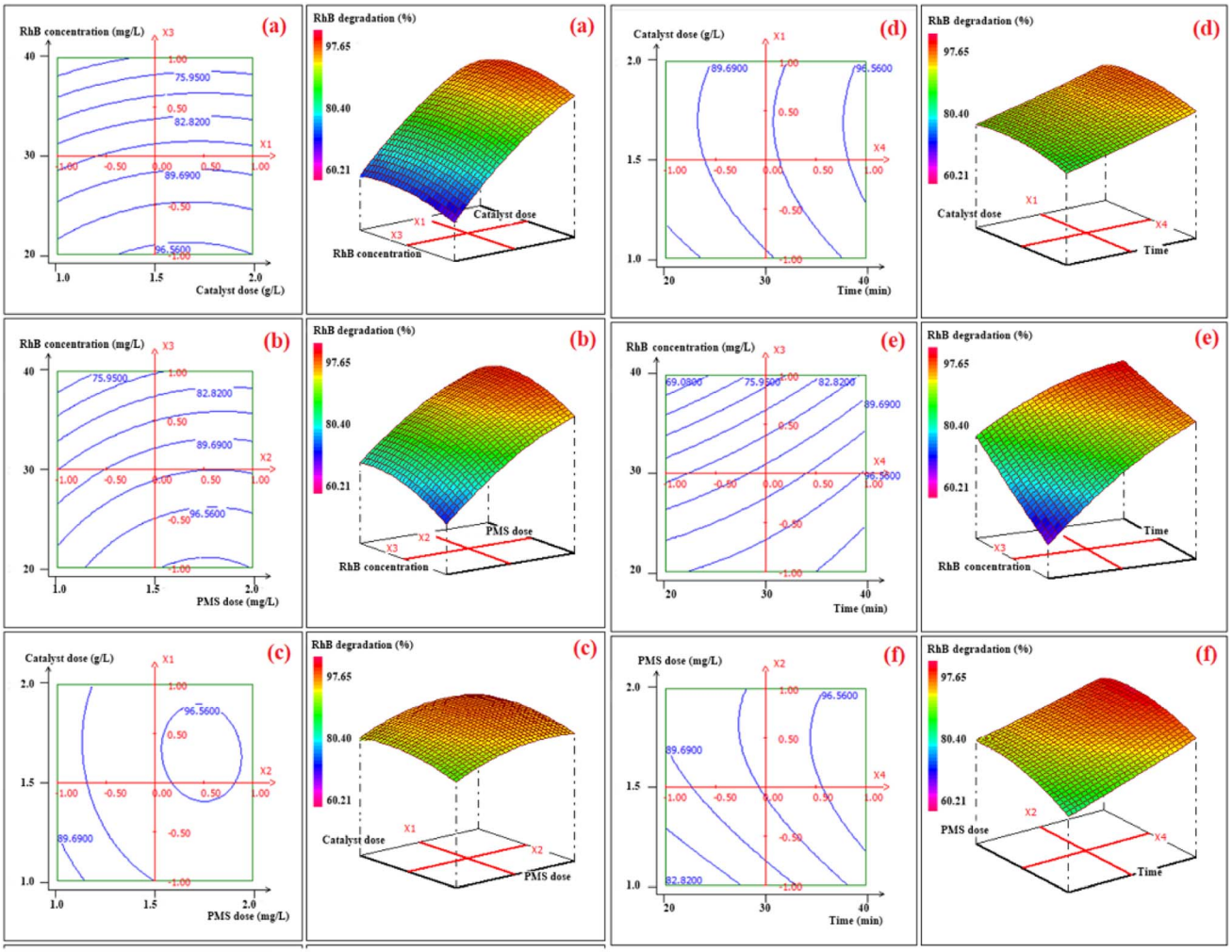

Fig. 4 2D–3D surface tracings showing the influence of the catalyst dose and RhB concentration. (a), PMS dose and RhB concentration (b), catalyst dose and PMS dose (c), catalyst dose and contact time (d), RhB concentration and contact time (e), PMS dose and contact time (f) on the RhB degradation efficiency (%).

response variation using *p*-values (Table S5†). The linear terms of the four factors, the quadratic terms (X_2^2 and X_3^2), and the interactive terms (X_2X_4 and X_3X_4) were found to have a *p*-value (less than 5%).[27,46] The regression coefficients analysis (Table S5†) shows that the most significant coefficients that have a synergetic effect on RhB degradation efficiency are the linear terms (X_1, X_2 and X_4), and the interactive term X_3X_4. On the other hand, the linear term X_3, the quadratic terms (X_2^2 and X_3^2), and the interaction term (X_2X_4) have an antagonist effect on the response (degradation efficiency). The 2D and 3D response surface plots in Fig. 4 illustrate the importance of the binary interactions between the chosen variables on RhB decomposition efficiency (%), namely catalyst mass, PMS mass, initial RhB concentration, and contact time.

For instance, it may be noticed from Fig. 4a that the RhB decomposition efficiency is greatly impacted by the RhB initial concentration while the catalyst dose has no significant effect on the response variation. Also, it can be observed from the Fig. 4f that the RhB degradation efficiency is highly influenced by the interaction effect of PMS dose and time. In accordance with these plots, the predicted value of optimal RhB degradation is (97.65 ± 1.80)% using 1 g l^{-1} of catalyst dose, 1 g l^{-1} of PMS dose, a RhB concentration of 25 mg l^{-1} for only 40 minutes of agitation. The chosen approach proved to be very efficient and the results achieved showed that the RSM-BBD method yielded high values of RhB degradation (%) according to several scenarios given by the software. As a result, the optimal operational parameters were employed to investigate the kinetics of RhB decomposition.

3.4. Catalytic activity of the $ZnCo_2O_4$/Alg/PMS

3.4.1. Catalytic behavior in a variety of oxidation operations. The decomposition of RhB was also studied in the presence of different catalysts at natural pH and the results are shown in Fig. 5. As we can clearly notice from this figure that the neat PMS system does not have the capability to degrade RhB which might be attributed to the fact that PMS is not able to be activated with no catalysts. When only $ZnCo_2O_4$/Alg was included, the degradation efficacy was significantly low

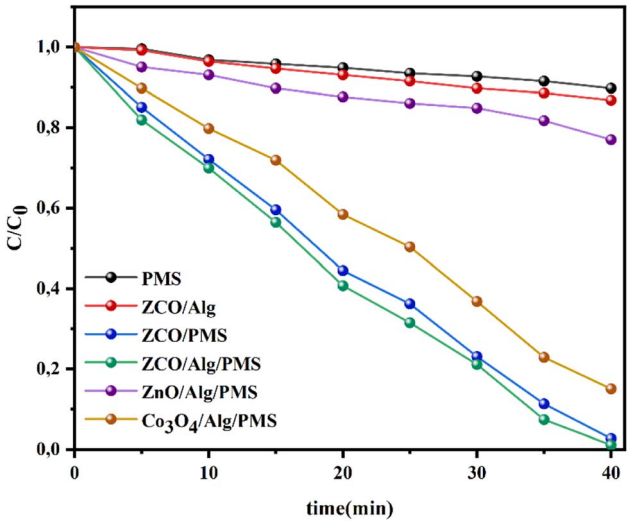

Fig. 5 degradation of RhB solutions in various systems. Initial concentrations: [RhB] = 25 mg l^{-1}, [catalyst] = 1 g l^{-1}, [PMS] = 1 g l^{-1}, ambient temperature.

(13.14%) within 40 min, which indicated that the $ZnCo_2O_4$/Alg catalyst is ineffective in degrading RhB. When $ZnCo_2O_4$/Alg NPs were employed with PMS, 98.87% of RhB was discolored in only 40 min, which is much better than that of the Co_3O_4/Alg/PMS and ZnO/Alg/PMS systems in which the respective discoloration efficiency of RhB is 84.94% and 22.95%, respectively. These comparative study indicate that the $ZnCo_2O_4$/Alg catalyst outperforms its oxide components (ZnO/Alg and Co_3O_4/Alg). The outstanding degradation performance of the $ZnCo_2O_4$/Alg/PMS system could stem from a number of aspects such as: (i) their small particle size (as calculated by the Debye–Scherrer equation and observed by TEM), (ii) the highest surface hydroxyl group density (as characterized *via* FTIR), (iii) the synergistic coupling of Zn–Co like already seen and proposed for Cu–Co,[55] Fe–Co.[56] However, encapsulation of $ZnCo_2O_4$ with alginate to form $ZnCo_2O_4$/Alg beads may retard the diffusion of RhB molecules inside the bead membranes, yet the availability of negative functional groups on alginates (OH and –COOH) is advantageous for the adsorption of the cationic dye, moreover the addition of alginate on $ZnCo_2O_4$ may enhance their chemical stability and separation capability.

3.4.2. Effect of pH and thermodynamic behavior investigation. Under the heterogeneous catalytic setup, the solution pH has a crucial role that influences the catalytic behavior.[57] Consequently, the influence of solution pH on RhB decomposition has been studied in the $ZnCo_2O_4$@Alg/PMS system. To make a detailed study of this effect, we regulated the pH of the solution to 3.2 and 11 at the temperature $T = 25$ °C, and under the optimum conditions found from the RSM study ([catalyst] = 1 g l^{-1}, [RhB] = 25 mg l^{-1}, [PMS] = 1 g l^{-1}). As illustrated in Fig. 6a, the catalytic decomposition is dependent on the pH value of the aqueous solutions of RhB, of which the greatest removal occurred at a pH equal to 7.5 with a removal efficiency of 98.28% within 30 min of reaction and a rate constant (k_{obs} = 0.1459 min^{-1}). The measurement of the point of zero charge (pH_{pzc}) of the $ZnCo_2O_4$/Alg catalyst (Fig. 6c), revealed that the surface of the material was negatively charged at pH > 7.2 and positively charged at pH < 7.2. In the same context the low degradation rate obtained at pH = 3.2 (44.92% with k_{obs} = 0.0141 min^{-1}) can be explained by the nature of RhB molecules which may have existed mostly as RhB^+, as RhB has a dissociation constant (pK_a) of 3.7, which resulted in electrostatic repulsion and hindered the adsorption of RhB onto the catalyst surface.[50,58]

This decrease may also be attributed to the H^+ ion scavenging effect for $SO^{\bullet -}$ and $OH^\bullet$ (eqn (5) and (6)), also a comparatively higher concentration of H^+ ions will restrict the dissociation of PMS and allow the formation of H_2SO_5 that will partially substitute HSO_5^-, thus lowering the electrostatic attraction between positively charged $ZnCo_2O_4$/Alg and PMS.[23,59]

$$SO_4^{\bullet -} + H^+ + e^- \rightarrow HSO_4^{\bullet -} \quad (5)$$

$$HO^\bullet + H^+ + e^- \rightarrow H_2O \quad (6)$$

It is also well documented that the acid H_2SO_5 with a $pK_{a_1} < 0$ corresponds to the reaction ($H_2SO_5 \leftrightarrow HSO_5^- + H^+$), while $pK_{a_2} \approx 9.4$ corresponds to the reaction ($HSO_5^- \leftrightarrow SO_5^{2-} + H^+$). PMS is mainly present in the form of SO_5^{2-} in strongly alkaline media (pH > 9.4), as HSO_5^- in acidic, neutral, and slightly alkaline solutions (pH < 9.4), and as both $HSO_5^-$and SO_5^{2-} at approximately pH 9.4.[60,61] Increasing the pH from 9.1 to 11 reduces the elimination rate of RhB due to the inhibitory effect of strongly alkaline media on PMS cleavage ($pK_a = 9.4$). At pH < 9.4, HSO_5^- ions dominate while SO_5^{2-} ions become dominant at higher pH.[50] The higher the alkalinity of the solution, the greater the electrostatic repulsion between the negative surface of the catalyst ($ZnCo_2O_4$/Alg) and PMS, resulting in lower activation of PMS on the catalyst surface,[62] and ultimately low catalytic activity at pH = 11. Additionally, under alkaline conditions, $SO4^{\bullet -}$ radicals can combine with hydroxyl anions (OH^-) to form a less potent oxidant, $HO^\bullet$, ($SO_4^{\bullet -} + HO^{\bullet -} \rightarrow SO_4^{2-} + HO^\bullet$).[63]

On the contrary, the impact of temperature on peroxymonosulfate activation is significant. Therefore, three distinct temperature values of 25, 35, and 45 °C were utilized to investigate the effect of PMS activation, which is shown in Fig. 6d. The findings indicate that at 45 °C, RhB degradation was accomplished in 12 minutes, demonstrating that temperature has a significant effect on the speed of oxidative degradation of RhB. Moreover, the degradation of RhB at various temperatures was described using the kinetic modulus of pseudo first order ($\ln(C/C_0) = -kt$) Fig. 6e, where C and C_0 denote the concentrations of RhB at time $t = t$ min and time $t = 0$, respectively. Here, k is the rate constant, and t is the reaction time in minutes. At 25 °C, the degradation constant for RhB was determined to be 0.1031 min^{-1} (R^2 = 0.9948), while at 35 °C and 45 °C, the degradation constants were 0.2859 min^{-1} (R^2 = 0.9886) and 0.5224 min^{-1} (R^2 = 0.9806), respectively. These findings can be attributed to the substantial liberation of $SO4^{\bullet -}$ radicals at higher temperatures. Additionally, by utilizing the Arrhenius equation (eqn (7)), it was possible to determine the activation

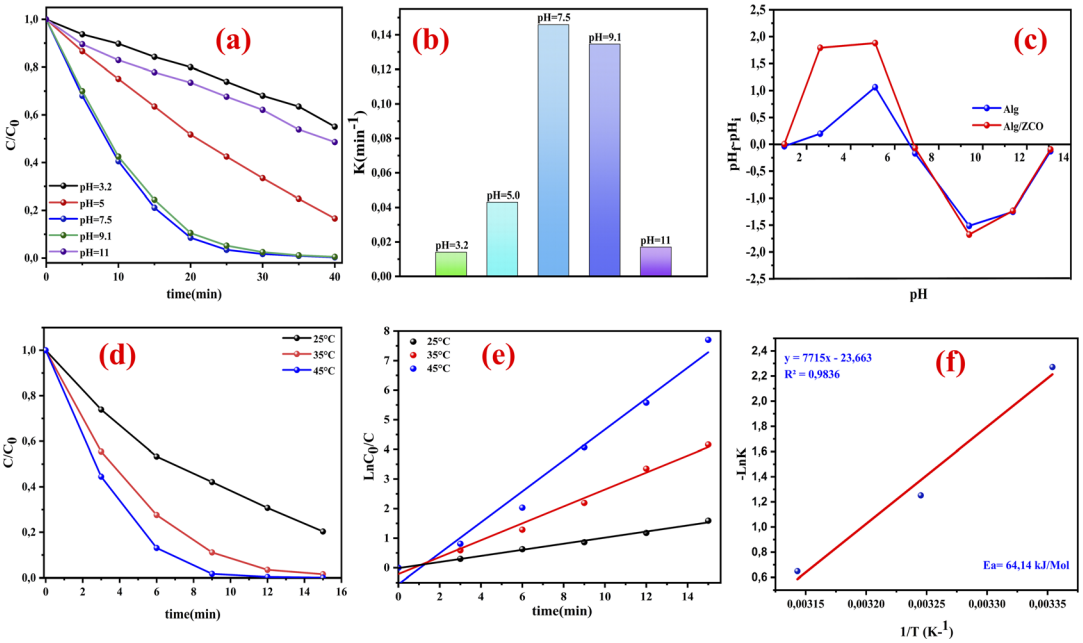

Fig. 6 (a) The influence of various pH values upon the decomposition of RhB. (b)The rate constant at different pH values. (c) The isoelectric point of Alg and ZCO/Alg at different pH. (d and e) Reaction temperature effects and activation energy (Ea) assessment for ZCO/Alg/PMS, (f)Arrhenius graph for RhB degradation using ZCO/Alg/PMS, [catalyst] = 1 g l^{-1}, [RhB] = 25 mg l^{-1}, [PMS] = 1 g l^{-1}.

energy (E_a) of the RhB degradation reaction on the $ZnCo_2O_4$/Alg catalyst.

$$\ln k = -E_a/RT + \ln A \quad (7)$$

A, which represents the frequency factor, is combined with R, the universal gas constant, and T, the temperature in Kelvin.[64] The graph displaying ln k *versus* $1/T$ illustrated a direct relationship, indicating a linear correlation between ln k and $1/T$ (with an R^2 value of 0.9836), as displayed in Fig. 6f. The calculated activation energy (E_a) was determined to be 64.14 kJ mol^{-1}. From this, it may be concluded that the temperature was beneficial for the decomposition of RhB.[65] Moreover, the calculated activation energy (E_a) value was considerably higher than the diffusion-controlled E_a values (ranging from 10–13 kJ mol^{-1}), implying that the observed reaction rate primarily depended on the chemical reaction rate of the $ZnCo_2O_4$/Alg surface, this is in agreement with previous reports.[66,67]

3.4.3. Effect of the amount of sodium alginate on the catalytic activity. The amount of sodium alginate can significantly influence the physicochemical properties and catalytic activity of the nanocomposites. To investigate this, a series of experiments were conducted by varying the amount of sodium alginate in the formulation (Fig. S6†). The ZCO weight was kept constant at 0.5 g in 100 ml of water to minimize costs and prevent interference with alginate bead formation. Although the catalyst with a 1/1 ratio showed good results, the stability of the beads was compromised, rendering it unsuitable for use. The results indicate that the percentage of sodium alginate has an adverse impact on the efficiency of ZCO. This can be attributed to sodium alginate acting as a barrier for rhodamine B, leading to a delay in its degradation, however the availability of negative functional groups on alginates (OH and –COOH) is advantageous for the adsorption of the cationic dye, moreover the addition of alginate on $ZnCo_2O_4$ may enhance their chemical stability and separation capability. Consequently, the experiment aimed to determine the optimal ratio by identifying the best-performing combination.

3.4.4. A comparative study of different oxidants (PMS, PS, and H_2O_2). Besides PMS, other studies have evaluated PS and H_2O_2 in AOPs.[68–70] In this study we have benchmarked the ability of $ZnCo_2O_4$/Alg NPs as a catalytic activator for the following oxidants (PMS, PS, H_2O_2) in the decomposition of RhB. As can be noticed in Fig. S7,† the decomposition efficacy of the $ZnCo_2O_4$/Alg/PMS, $ZnCo_2O_4$/Alg/PS and $ZnCo_2O_4$/Alg/H_2O_2 systems was 98.48%, 71.16% and 48.45% respectively. The greater oxidative potencies of the former two systems could be related to the fact which O–O bond energy within PMS (140 < E_{PMS} < 213.3) and PS (140 kJ mol^{-1}) is smaller as compared to H_2O_2 (213.3 kJ mol^{-1}), which renders the activation of PS and PMS energetically easier. Although the PMS oxidation potential (1.82 V) is smaller than that of PS (2.01 V), the degradation rate of PMS is greater than that of PS, this was caused by the non-symmetric PMS structure which seems to render it more readily activated.[71]

3.4.5. Stability of the $ZnCo_2O_4$/Alg catalyst. One of the problems in wastewater processing is the durability of the catalyst activity throughout the depollution procedure. Therefore, with the aim of verifying the recycling effectiveness of the catalyst employed within this study, reuse tests have been carried out. Due to its shape the catalyst may be separated

readily from the reaction mixture after each round, the results are given in Fig. 7a. After repeating the procedure 5 times, the catalyst efficiency slowly reduced from 98% to 78% of discoloration. The insignificant decrease in performance after the fifth run can be associated with: (i) the covering of the active sites onto the surface of the catalyst. (ii) Low losse of activator elements in the separation/drying operation prior to the following cycle. The FTIR analysis (Fig. 7b) proves the stability of the $ZnCo_2O_4$/Alg catalyst, since there are no changes in the bands corresponding to the $ZnCo_2O_4$ and the polymer after their reuses. These findings are indicative of the excellent stability and reusability of the $ZnCo_2O_4$/Alg catalyst. In addition to their stability, the newly developed hydrogel beads catalysts are effective against RhB degradation, easily prepared, environmentally friendly, recyclable and therefore have potential future industrial applications.

3.4.6. RhB mineralization by COD analysis. COD analyses were performed to illuminate the mineralization during the catalyst/PMS/dye operation. As illustrated in Fig. 8a and b the COD removal efficiency at 40 min was 82%. It is well noticed that the color reduction was higher compared to COD in this setup that is similar with other research.[72] This might be justified based on the fact that the intermediates are tougher to decompose and their oxidation rate could be substantially slower than those of the original compound.[73,74] Besides, it can be concluded that the use of the ZCO/PMS catalyst resulted in an acceptable removal efficiency per COD which shows the ability of the catalyst to activate the PMS and generate a surplus of hydroxyl and sulfate radicals.

3.4.7. The proposed mechanism. PMS can be catalyzed by $ZnCo_2O_4$/Alg to yield $SO_4^{\bullet-}$ and $OH^{\bullet}$ radicals. To find out the catalytic behavior of every free radical upon the decomposition of RhB, chemical deactivation tests of *tert*-butyl alcohol (*t*-BA) and ethanol (EtOH) were independently added in to the experimental system as deactivating agents. A number of investigations have been made in the literature demonstrating that alpha hydrogen-containing alcohols like EtOH may react readily with $OH^{\bullet}$ and $SO_4^{\bullet-}$ radicals,[75,76] and are capable of scavenging both $OH^{\bullet}$ with ($k = (1.2–2.8) \times 10^9\ M^{-1}\ s^{-1}$) and $SO_4^{\bullet-}$ with ($k = (1.6–7.7) \times 10^7\ M^{-1}\ s^{-1}$).[57,77] Whereas *t*-BA is regarded as a trapper of $OH^{\bullet}$ radicals solely with ($k = (3.8–7.6) \times 10^8\ M^{-1}\ s^{-1}$).[78,79] As depicted in Fig. S8a,† the quenching tests are given in the form of a reaction rate constant. When a concentration of 1 mmol l^{-1} *t*-BA and EtOH were added into the combined $ZnCo_2O_4$/Alg system, the RhB elimination rates were reduced to 85% and 50%, respectively and the kinetic constants were dropped (Fig. S8b†). Within the presence of EtOH there was a considerable decrease of the RhB, indicating that the $OH^{\bullet}$ and $SO_4^{\bullet-}$ radicals were caught by the alcohol molecules, whereas a slight decrease of the RhB was observed when using *t*-BA. Outcomes clearly reveal that the main dominant radical involved in the decomposition process is $SO_4^{\bullet-}$ while $OH^{\bullet}$ radicals can also be included; however, their participation is negligible in comparison to $SO_4^{\bullet-}$ radicals. Besides $SO_4^{\bullet-}$ and $OH^{\bullet}$ radicals, the superoxide intermediate ($O_2^{\bullet-}$) also plays an influential role as a reactive species in the free radical oxidation reaction. The $O_2^{\bullet-}$ scavenging tests were carried out using *p*-benzoquinone (*p*-BQ) as a selective quencher with high reaction rate toward $O_2^{\bullet-}$ ($k = 9 \times 10^8\ M^{-1}\ s^{-1}$).[80,81] Fig. S8a and b† indicate that the catalytic activities of ZCO/Alg are slightly reduced after the addition of *p*-BQ, and the reaction rate constant is weakly attenuated from 0.0959 min^{-1} (no quencher) to 0.0706 min^{-1}, indicating that $O_2^{\bullet-}$ is not the dominant ROS in the ZCO/Alg system. Based on the previously mentioned findings, the heterogeneous activation mechanism of PMS by $ZnCo_2O_4$/Alg is offered in Scheme 1. According to the findings of the catalytic activity, the probable

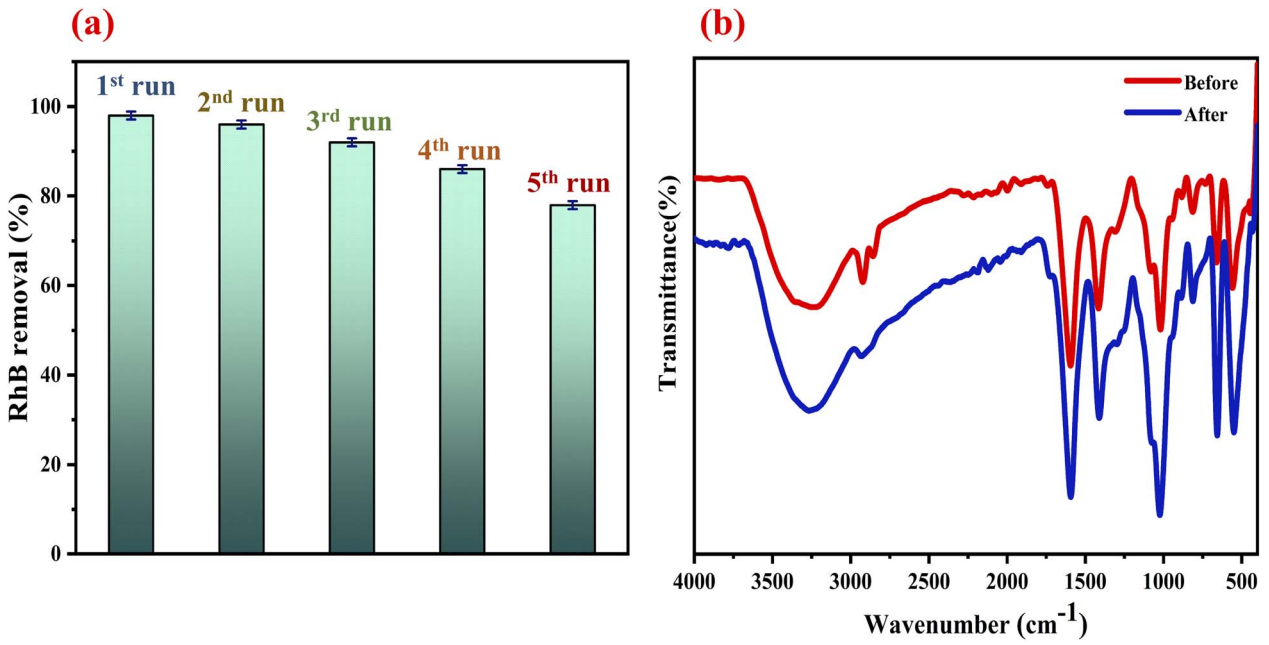

Fig. 7 (a) Recycling test of the ZCO/Alg catalyst. (b) FTIR spectrum of the ZCO/Alg before and after RhB degradation.

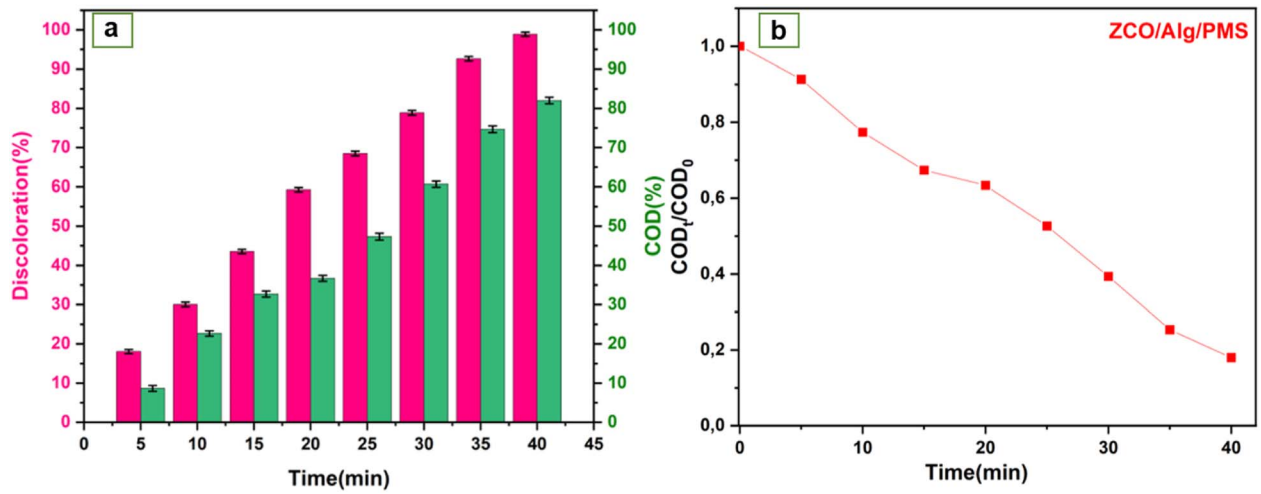

Fig. 8 (a and b) Analysis of chemical oxygen demand (COD) *versus* time using ZCO/Alg catalyst under the conditions, [catalyst] = 1 g l^{-1}, [RhB] = 25 mg l^{-1}, [PMS] = 1 g l^{-1}, ambient temperature.

mechanism of PMS activation by $ZnCO_2O_4$/Alg alginate beads may be proposed as described in the following reactions.[27,82] First of all, the Co^{2+} bound to the surface might activate HSO_5^- for generating $SO_4^{\bullet -}$ and Co^{3+} (eqn (8)). The resulting Co^{3+} might return to Co^{2+} through the reaction between Co^{3+} and HSO_5^-, generating $SO_5^{\bullet -}$ (eqn (9)). Besides, the generated OH^- ions are tending to react with the $SO_4^{\bullet -}$ radicals to form the hydroxyl radicals $OH^{\bullet}$ (eqn (10)). The resulting $SO_4^{\bullet -}$ and $OH^{\bullet}$ radicals would potentially oxidize RhB to small molecules and then to inorganic substances (eqn (11) and (12)).

$$HSO_5^- + Co^{2+} \rightarrow Co^{3+} + OH^- + SO_4^{\bullet -} \quad (8)$$

$$HSO_5^- + Co^{3+} \rightarrow Co^{2+} + SO_5^{\bullet -} + H^+ \quad (9)$$

$$SO_4^{\bullet -} + OH^- \rightarrow SO_4^{2-} + OH^{\bullet} \quad (10)$$

$$SO_4^{\bullet -}/OH^{\bullet} + RhB \rightarrow \text{Intermediate product} \quad (11)$$

$$SO_4^{\bullet -}/OH^{\bullet} + \text{Intermediate product} \rightarrow CO_2 + H_2O \quad (12)$$

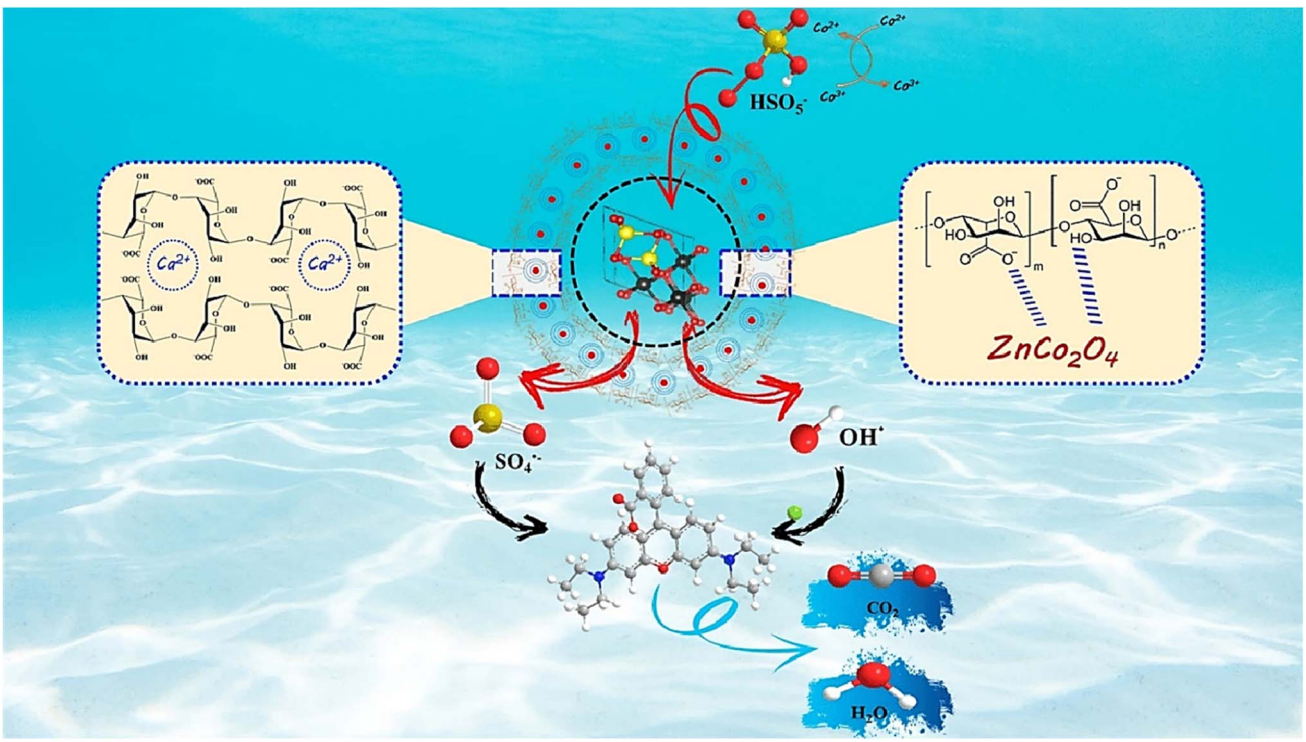

Scheme 1 Mechanism of peroxymonosulfate (PMS) activation on ZCO@Alg.

Table 1 Comparative evaluation of catalysts for RhB degradation through PMS activation

System	RhB concentration (ppm)	Catalyst dose (g l^{-1})	Reaction time (min)	Removal efficiency (%)	Ref.
$CoTiO_3$@Co_3O_4	50	0.5	60	100	85
α-MnO_2/Pal	20	0.1	180	Nearly 100	86
$CoFe_2O_4$	20	0.5	40	66.2	87
30%-CNTs-Fe-Mn-0.5	15	0.1	60	95	88
N-$CuMe_2$Pc/siloxene	20	0.1	60	95.3	89
$BiFeO_3$	5	1	40	>60	90
CoFe/SBA-15	5	0.1	120	>95	91
5% Ca–Fe_2O_3	10	1	120	99	84
NiO-$NiFe_2O_4$-rGO	20.16	1.5	40	100	83
$ZnCo_2O_4$/Alg	25	1	40	98	This study

3.4.8. Comparison with catalyst systems described in the literature. The competitiveness of the currently developed catalyst has been examined in comparison to different catalysts mentioned in the literature for their RhB degradation efficiency *via* PMS activation, as illustrated in Table 1. As shown in Table 1, our produced catalyst exhibited highly competitive RhB degradation compared to other systems, such as NiO-$NiFe_2O_4$-rGO (where 1.5 g l^{-1} of the catalyst degraded 20 ppm of RhB within 40 minutes),[83] and 5% Ca–Fe_2O_3 (achieving 99% degradation using 1 g l^{-1} of the catalyst for 120 minutes).[84] Taking into account all the advantages and disadvantages of the reported catalyst systems, it is evident that the currently developed catalyst demonstrates a moderate degradation efficiency compared to other systems that required a recovery step either through centrifugation or magnetic separation.

4 Conclusions

This paper outlines a pathway for the manufacture of novel bionanocomposite based on $ZnCo_2O_4$/Alg. The prepared ZCO coated with alginate was found to be capable of activating PMS and generating a large quantity of sulfate radicals able to decompose RhB molecules. The several key factors, including the RhB concentration, the dose of ZCO/Alg, the dose of PMS and the reaction time were mathematically investigated using a statistical tool called RSM. RhB decomposition efficacy of 98% was reached for the optimized conditions of a PMS dose of 1 g l^{-1}, the catalyst dose of 1 g l^{-1}, dye concentration of 25 mg l^{-1} and a time of 40 min. The trapping tests showed that the $SO_4^{\bullet-}$ radical plays a more critical function in the decomposition studies of RhB. Moreover, The $ZnCo_2O_4$/Alg catalyst has shown excellent stability and reusability based on recycling tests. The employment of ZCO/Alg composite as catalyst for the activation of PMS can be considered as a future efficient material for the organic contaminants deterioration and the sewage treatment through the decomposition procedure.

Author contributions

Badr-Eddine Channab: writing the draft, data curation; formal analysis. Mohammed El Ouardi: writing the draft, data curation; formal analysis. Salah Eddine Marrane: writing, formal analysis. OMAR. Ait Layachi: writing, review & editing. Ayoub El Idrissi: writing, formal analysis. Salaheddine Farsad: review & editing. Driss Mazkad: formal analysis. Amal BaQais: review & editing. Mohammed Lasri: SEM/EDS formal analysis. Hassan Ait Ahsaine: project administration; supervision and validation.

Conflicts of interest

The authors report that they have no known conflicts of interest.

Acknowledgements

The authors sincerely thank the University Hassan II, Casablanca, Mohammed V University in Rabat and University Ibn Zohr, Agadir, for their engagement and support of young researchers for developing international works. A. B want to thank Princess Nourah bint Abdulrahman University Researchers Supporting Project number (PNURSP2023R230), Princess Nourah bint Abdulrahman University, Riyadh, Saudi Arabia.

References

1 M. R. Abukhadra, A. Adlii and B. M. Bakry, *Int. J. Biol. Macromol.*, 2019, **126**, 402–413.
2 I. Dalponte Dallabona, Á. L. Mathias and R. M. M. Jorge, *Colloids Surf., A*, 2021, **627**, 127159.
3 L. Nouri, S. Hemidouche, A. Boudjemaa, F. Kaouah, Z. Sadaoui and K. Bachari, *Int. J. Biol. Macromol.*, 2020, **151**, 66–84.
4 A. Asghari, M. Hemati, M. Ghaedi, M. Rajabi and B. Mirtamizdoust, *J. Nanostruct.*, 2014, **4**, 17–30.
5 Y. Wang, Y. Gong, N. Lin, L. Yu, B. Du and X. Zhang, *J. Colloid Interface Sci.*, 2022, **606**, 941–952.
6 M. El Ouardi, A. El aouni, H. A. Ahsaine, M. Zbair, A. BaQais and M. Saadi, *Chemosphere*, 2022, 136483.
7 A. Elaouni, M. E. Ouardi, M. Zbair, A. BaQais, M. Saadi and H. A. Ahsaine, *RSC Adv.*, 2022, **12**, 31801–31817.
8 H. Li, J. Yu, Y. Gong, N. Lin, Q. Yang, X. Zhang and Y. Wang, *Sep. Purif. Technol.*, 2023, **307**, 122716.
9 J. Yu, H. Li, N. Lin, Y. Gong, H. Jiang, J. Chen, Y. Wang and X. Zhang, *Catalysts*, 2023, **13**, 148.

10 S. Giannakis, K.-Y. A. Lin and F. Ghanbari, *Chem. Eng. J.*, 2021, **406**, 127083.
11 N. Liu, Y. Dang, B. Hu, M. Tian, H. Jiang, G. Quan, R. Qiao, J. Lei and X. Zhang, *Surf. Interfaces*, 2022, **35**, 102472.
12 A. Ait El Fakir, Z. Anfar, A. Amedlous, M. Zbair, Z. Hafidi, M. El Achouri, A. Jada and N. El Alem, *Appl. Catal., B*, 2021, **286**, 119948.
13 B. Li, Y.-F. Wang, L. Zhang and H.-Y. Xu, *Chemosphere*, 2022, **291**, 132954.
14 F. Liu, J. Cao, Z. Yang, W. Xiong, Z. Xu, P. Song, M. Jia, S. Sun, Y. Zhang and X. Zhong, *J. Colloid Interface Sci.*, 2021, **581**, 195–204.
15 J. Hu, X. Zeng, Y. Yin, Y. Liu, Y. Li, X. Hu, L. Zhang and X. Zhang, *Environ. Sci.: Nano*, 2020, **7**, 3547–3556.
16 A. Ait El Fakir, Z. Anfar, M. Benafqir, A. Jada and N. El Alem, *J. Chem. Technol. Biotechnol.*, 2019, **94**, 2609–2620.
17 J. Yao, X. Zeng and Z. Wang, *Chem. Eng. J.*, 2017, **330**, 345–354.
18 K. Missaoui, R. Ouertani, E. Jbira, R. Boukherroub and B. Bessaïs, *Environ. Sci. Pollut. Res.*, 2021, **28**, 52236–52246.
19 I. Othman, J. Hisham Zain, M. Abu Haija and F. Banat, *Appl. Catal., B*, 2020, **266**, 118601.
20 Z. Xiao, Y. Li, L. Fan, Y. Wang and L. Li, *J. Colloid Interface Sci.*, 2021, **589**, 298–307.
21 L. Liu, Y. Li, Y. Pang, Y. Lan and L. Zhou, *Chem. Eng. J.*, 2020, **401**, 126014.
22 X. Tian, C. Tian, Y. Nie, C. Dai, C. Yang, N. Tian, Z. Zhou, Y. Li and Y. Wang, *Chem. Eng. J.*, 2018, **331**, 144–151.
23 M. Xu, H. Zhou, Z. Wu, N. Li, Z. Xiong, G. Yao and B. Lai, *J. Hazard. Mater.*, 2020, **399**, 123103.
24 X. Wang, J. Jiang, Y. Ma, Y. Song, T. Li and S. Dong, *J. Colloid Interface Sci.*, 2021, **600**, 449–462.
25 J. Huang, Y. Wang, K. Chen, T. Liu and Q. Wang, *Chin. Chem. Lett.*, 2022, **33**, 2060–2064.
26 J. Yu, L. Lu, J. Li and P. Song, *RSC Adv.*, 2016, **6**, 12797–12808.
27 L. Hu, G. Zhang, M. Liu, Q. Wang and P. Wang, *Chemosphere*, 2018, **212**, 152–161.
28 Y. Gao and D. Zou, *Chem. Eng. J.*, 2020, **393**, 124795.
29 Y. Gao, S. Cong, H. Yu and D. Zou, *Sep. Purif. Technol.*, 2021, **262**, 118330.
30 H. Dong, G. Zeng, L. Tang, C. Fan, C. Zhang, X. He and Y. He, *Water Res.*, 2015, **79**, 128–146.
31 Z. Anfar, A. Amedlous, A. A. El Fakir, M. Zbair, H. Ait Ahsaine, A. Jada and N. El Alem, *Chemosphere*, 2019, **236**, 124351.
32 S. Rezgui, A. M. Díez, L. Monser, N. Adhoum, M. Pazos and M. A. Sanromán, *J. Environ. Manage.*, 2021, **283**, 111987.
33 N. M. Velings and M. M. Mestdagh, *Polym. Gels Networks*, 1995, **3**, 311–330.
34 C. A. A. Pereira, M. R. Nava, J. B. Walter, C. E. Scherer, A. Dominique Kupfer Dalfovo and M. Barreto-Rodrigues, *J. Hazard. Mater.*, 2021, **401**, 123275.
35 G. Grant, E. Morris, D. Rees, P. J. C. Smith and D. Thom, *FEBS Lett.*, 1973, **32**, DOI: 10.1016/0014-5793(73)80770-7.
36 Y. Zhuang, F. Yu, J. Chen and J. Ma, *J. Environ. Chem. Eng.*, 2016, **4**, 147–156.
37 E. Amaterz, A. Bouddouch, A. Tara, A. Taoufyq, Z. Anfar, B. Bakiz, L. Bazzi, A. Benlhachemi and O. Jbara, *Electrocatalysis*, 2020, **11**, 642–654.
38 Z. Anfar, H. Ait Ahsaine, M. Zbair, A. Amedlous, A. Ait El Fakir, A. Jada and N. El Alem, *Crit. Rev. Environ. Sci. Technol.*, 2020, **50**, 1043–1084.
39 J. Yao, Y. Zhang and Z. Dong, *Chem. Eng. J.*, 2021, **415**, 128938.
40 Y. Yang, Z. Zheng, W. Ji, J. Xu and X. Zhang, *J. Hazard. Mater.*, 2020, **395**, 122686.
41 B. Bouzayani, E. Rosales, M. Pazos, S. C. Elaoud and M. A. Sanromán, *J. Cleaner Prod.*, 2019, **228**, 222–230.
42 W. S. Wan Ngah, *J. Environ. Manage.*, 2010, **91**, 958–969.
43 X. Song, Q. Ru, B. Zhang, S. Hu and B. An, *J. Alloys Compd.*, 2014, **585**, 518–522.
44 S. Vijayanand, P. A. Joy, H. S. Potdar, D. Patil and P. Patil, *Sens. Actuators, B*, 2011, **152**, 121–129.
45 S. Hua, H. Ma, X. Li, H. Yang and A. Wang, *Int. J. Biol. Macromol.*, 2010, **46**, 517–523.
46 T. Lu, T. Xiang, X.-L. Huang, C. Li, W.-F. Zhao, Q. Zhang and C.-S. Zhao, *Carbohydr. Polym.*, 2015, **133**, 587–595.
47 B. Rashidzadeh, E. Shokri, G. R. Mahdavinia, R. Moradi, S. Mohamadi-Aghdam and S. Abdi, *Int. J. Biol. Macromol.*, 2020, **154**, 134–141.
48 V. Uddin Siddiqui, A. Ansari, M. Taazeem Ansari, M. Khursheed Akram and W. Ahmad Siddiqi, *RSC Adv.*, 2022, **12**, 7210–7228.
49 Y. Naciri, H. Ait Ahsaine, A. Chennah, A. Amedlous, A. Taoufyq, B. Bakiz, M. Ezahri, S. Villain and A. Benlhachemi, *J. Environ. Chem. Eng.*, 2018, **6**, 1840–1847.
50 D. Wei, Y. Liu, Y. Song, W. Liu, L. Zhao, L. Wang, R. Wu and C. Yang, *J. Chem. Technol. Biotechnol.*, 2021, **96**, 1936–1946.
51 M. A. Alrebaki, M. M. Ba-Abbad and A. Z. Abdullah, *Arabian J. Sci. Eng.*, 2023, **48**, DOI: 10.1007/s13369-022-07577-9.
52 Y. Sharma, N. Sharma, G. V. Subba Rao and B. V. R. Chowdari, *Adv. Funct. Mater.*, 2007, **17**, 2855–2861.
53 A. Amjlef, S. Farsad, A. Ait El Fakir, A. El Asri, S. El Issami, S. Et-Taleb and N. El Alem, *Ceram. Int.*, 2023, **49**, 14120–14134.
54 Y. Yang, X. Li, Y. Gu, H. Lin, B. Jie, Q. Zhang and X. Zhang, *Surf. Interfaces*, 2022, **28**, 101649.
55 C. Chen, L. Liu, Y. Li, W. Li, L. Zhou, Y. Lan and Y. Li, *Chem. Eng. J.*, 2020, **384**, 123257.
56 H. Wang, C. Wang, J. Qi, Y. Yan, M. Zhang, X. Yan, X. Sun, L. Wang and J. Li, *Nanomaterials*, 2019, **9**, 402.
57 N. Trung Dung, T. Viet Thu, T. V. Nguyen, B. Minh Thuy, M. Hatsukano, K. Higashimine, S. Maenosono and Z. Zhong, *RSC Adv.*, 2020, **10**, 3775–3788.
58 J. Deng, Y.-J. Chen, Y.-A. Lu, X.-Y. Ma, S.-F. Feng, N. Gao and J. Li, *Environ. Sci. Pollut. Res.*, 2017, **24**, 14396–14408.
59 Y. Hong, J. Peng, X. Zhao, Y. Yan, B. Lai and G. Yao, *Chem. Eng. J.*, 2019, **370**, 354–363.
60 F. Ghanbari and M. Moradi, *Chem. Eng. J.*, 2017, **310**, 41–62.
61 Y.-H. Guan, J. Ma, Y.-M. Ren, Y.-L. Liu, J.-Y. Xiao, L. Lin and C. Zhang, *Water Res.*, 2013, **47**, 5431–5438.
62 Y.-H. Guan, J. Ma, X.-C. Li, J.-Y. Fang and L.-W. Chen, *Environ. Sci. Technol.*, 2011, **45**, 9308–9314.

63 P. Hu and M. Long, *Appl. Catal., B*, 2016, **181**, 103–117.
64 Y. Yao, Z. Yang, D. Zhang, W. Peng, H. Sun and S. Wang, *Ind. Eng. Chem. Res.*, 2012, **51**, 6044–6051.
65 Y. Leng, W. Guo, X. Shi, Y. Li and L. Xing, *Ind. Eng. Chem. Res.*, 2013, **52**, 13607–13612.
66 J. Deng, S. Feng, K. Zhang, J. Li, H. Wang, T. Zhang and X. Ma, *Chem. Eng. J.*, 2017, **308**, 505–515.
67 J. Deng, Y. Cheng, Y. Lu, J. C. Crittenden, S. Zhou, N. Gao and J. Li, *Chem. Eng. J.*, 2017, **330**, 505–517.
68 A. Ait El Fakir, Z. Anfar, M. Enneiymy, A. Jada and N. El Alem, *Appl. Catal., B*, 2022, **300**, 120732.
69 X. Ding, L. Gutierrez, J.-P. Croue, M. Li, L. Wang and Y. Wang, *Chemosphere*, 2020, **253**, 126655.
70 A. A. Márquez, I. Sirés, E. Brillas and J. L. Nava, *Chemosphere*, 2020, **259**, 127466.
71 L. Chen, X. Zuo, L. Zhou, Y. Huang, S. Yang, T. Cai and D. Ding, *Chem. Eng. J.*, 2018, **345**, 364–374.
72 F. Ghanbari, M. Khatebasreh, M. Mahdavianpour, A. Mashayekh-Salehi, E. Aghayani, K.-Y. A. Lin and B. K. Noredinvand, *Korean J. Chem. Eng.*, 2021, **38**, 1416–1424.
73 C. Cai, H. Zhang, X. Zhong and L. Hou, *Water Res.*, 2014, **66**, 473–485.
74 H. Zhang, J. Wu, Z. Wang and D. Zhang, *J. Chem. Technol. Biotechnol.*, 2010, **85**, 1436–1444.
75 P. Hu, H. Su, Z. Chen, C. Yu, Q. Li, B. Zhou, P. J. J. Alvarez and M. Long, *Environ. Sci. Technol.*, 2017, **51**, 11288–11296.
76 P. Shi, R. Su, F. Wan, M. Zhu, D. Li and S. Xu, *Appl. Catal., B*, 2012, **123–124**, 265–272.
77 G. P. Anipsitakis and D. D. Dionysiou, *Environ. Sci. Technol.*, 2004, **38**, 3705–3712.
78 C. Tan, N. Gao, Y. Deng, J. Deng, S. Zhou, J. Li and X. Xin, *J. Hazard. Mater.*, 2014, **276**, 452–460.
79 X. Yue, W. Guo, X. Li, H. Zhou and R. Wang, *Environ. Sci. Pollut. Res.*, 2016, **23**, 15218–15226.
80 K. Zhu, Y. Shen, J. Hou, J. Gao, D. He, J. Huang, H. He, L. Lei and W. Chen, *Chem. Eng. J.*, 2021, **412**, 128521.
81 S. Zhu, C. Jin, X. Duan, S. Wang and S.-H. Ho, *Chem. Eng. J.*, 2020, **393**, 124725.
82 Y. Yang, G. Banerjee, G. W. Brudvig, J.-H. Kim and J. J. Pignatello, *Environ. Sci. Technol.*, 2018, **52**, 5911–5919.
83 X. Xu, Y. Li, G. Zhang, F. Yang and P. He, *Water*, 2019, **11**, 384.
84 S. Guo, H. Wang, W. Yang, H. Fida, L. You and K. Zhou, *Appl. Catal., B*, 2020, **262**, 118250.
85 H. Li, Q. Gao, G. Wang, B. Han, K. Xia and C. Zhou, *Appl. Surf. Sci.*, 2021, **536**, 147787.
86 C. Huang, Y. Wang, M. Gong a, W. Wang, Y. Mu and Z. Hu Hu, *Sep. Purif. Technol.*, 2020, **230**, 115877.
87 P. Niu, C. Li, C. Jia, D. Wang and S. Liu, *J. Sol-Gel Sci. Technol.*, 2020, **93**, 419–427.
88 X. Tian and L. XiaoJ, *Colloid Interface Sci.*, 2020, **580**, 803–813.
89 M. Li, W. Wang, R. Ramachandran, F. Chen and Z.-X. Xu, *J. Photochem. Photobiol., A*, 2023, **441**, 114702.
90 F. Chi, B. Song, B. Yang, Y. Lv, S. Ran and Q. Huo, *RSC Adv.*, 2015, **5**, 67412–67417.
91 L. Hu, F. Yang, L. Zou, H. Yuan and X. Hu, *Chin. J. Catal.*, 2015, **36**, 1785–1797.